SEMARAK ILMU PUBLISHING

Semarak Engineering Journal

Journal homepage:
https://semarakilmu.my/index.php/sej/index
ISSN: 3036-0145

Floquet Analysis and Symmetry Breaking Flow Patterns of a Thin Plunging Rectangular Plate

Nitin Kumar[1,*], Nipun Arora[2], Amit Gupta[3], Sanjeev Sanghi[4]

[1] Department of Mechanical Engineering, GBPIET, Pauri-Garhwal, Uttarakhand, 246194, India
[2] Department of Mechanical Engineering, Indian Institute of Technology Jodhpur, Jodhpur, 342037, India
[3] Department of Mechanical Engineering, Indian Institute of Technology Delhi, New Delhi, 110016, India
[4] Department of Applied Mechanics, Indian Institute of Technology Delhi, New Delhi, 110016, India

ARTICLE INFO

Article history:
Received 9 March 2025
Received in revised form 15 April 2025
Accepted 24 May 2025
Available online 30 June 2025

Keywords:
Lattice Boltzmann method; Floquet analysis; plunging; instability; self-propulsion

ABSTRACT

The present study focuses on the development of a numerical framework for predicting the horizontal movement of a vertically plunging plate due to symmetry breaking in the flow, mimicking the flight of a flapping insect wing. The wing is represented as a thin, rigid rectangular plate plunging in a quiescent fluid. Numerical simulations are performed on the unconstrained plunging rectangular plate (i.e., free to propel along a direction orthogonal to the plunging direction) by utilizing a translating continuous-grid-block and multiple-relaxation time variant of the lattice Boltzmann method. The onset of asymmetry is identified by the critical values of non-dimensional amplitude (represented by Keulegan-Carpenter number, *KC*) and frequency (or Stokes number, β) and thickness to chord ratio (δ). The flow asymmetry that leads to self-propulsion is assessed by formulating an eigenvalue problem using Floquet analysis. It is shown that conditions for which propulsion initiates can be identified in a time-effective manner using the developed Floquet framework rather than a rigorous binary search-based method. Our analysis shows that the transition boundary in *KC*-β space shifts to smaller KC for given β as δ is reduced, suggesting that breaking of symmetry is readily achieved for a plate with lower δ. Furthermore, we report four distinct trajectories of the plate that depend on the combination of KC and β. While the plate exhibits unidirectional propulsion for large β, oscillatory motion is observed when *KC* >2 and β <20. These kinematics are further differentiated using flow patterns associated with the plunging plate during propulsion and the phase-portraits of the coefficient of horizontal thrust. By probing the effect of ground clearance (ς) on the propulsion of the plate, it is shown that the shed vortices from the plate reflect from the nearby wall and reduce the effective circulation around the plunging plate leading to a delay in onset of instability. Meanwhile, lack of this plate-wake interaction results in flow asymmetry being observed much earlier for a plate that is far away from the stationary wall.

* *Corresponding author.*
E-mail address: nitinbali100@gmail.com

https://doi.org/10.37934/sej.9.1.5475

1. Introduction

Nature's flyers (birds, bats, and insects) have evolved over the past 150 million years and possess an impressive biological flight where flapping of wings is utilized to not only generate lift but also forward thrust [1-4]. Unlike large manned vehicles, the biological flyers usually operate at a low Reynolds number (*Re*) that has adverse aerodynamic conditions (i.e., low lift-to-drag ratio). At large length scales, flapping becomes redundant as the lift can be easily generated by deriving forward motion through an engine via either propellers or high-velocity jets, as in conventional fixed-wing aircraft. Thus, the flying capability of insects at low speed has motivated researchers to develop micro air vehicles (MAVs) with a characteristic dimension of 15 cm or smaller and flight speed of 10m/s or lower [5,6,8]. When equipped with a payload, camera or sensor, these can be used to collect valuable information to perform tasks such as reconnaissance, surveillance and patrolling in restricted areas that may not be otherwise possible. Thus, they have rapidly evolved as trendy defence gadgets with conditions of stable hover, high maneuverability, vertical take-off/landing capability and quiet locomotion. Rapid advancements in material science, electronics and corresponding innovations and size reduction of power sources have further contributed to the commercialization of these MAVs [8].

Knoller [9] and Betz [8] were the first ones to observe the phenomenon of thrust generation in birds. They investigate that vertically heaving airfoil creates an effective angle of attack which provides a normal force vector in the horizontal direction and is responsible for thrust generation, which was later tentatively demonstrated by Katzmayr [10]. The above study by Knoller [9] and Beta [8] on a rigid plunging wing that either flaps the wing in a fixed position with the oncoming flow or cruises through the flow was later supported by numerous experiments and computational examinations [11-16]. Going further, the present study has been conducted on a self-propelled rigid wing (the forward translation is produced only by a flapping motion and both are interdependent or linked) to mimic the action of a biological flyer.

A portion of the vital findings of past studies on a self-propulsion wing [17-25] are summarized here. Vandenberghe *et al.,* [23, 24] experimentally showed that the symmetry breaking of a periodic motion at a critical Reynolds number (Re_c) leads to forward flapping flight. Alben and Shelly [17] revealed that the imposed oscillations of a two-dimensional ellipse could lead to forward propulsion in two stages. First, the fluid flow loses symmetry due to the linear instability. Second, nonlinear fluid-solid interactions between the body and previously shed vortices push the body into forward propulsion. It was also reported that Re_c for the onset of such thrust is independent of the density ratio ($\rho^* = \rho_s / \rho_f$) , where ρ_s is the density of the solid body and ρ_f is the fluid density. Lu and Liao [22] predicted the critical Reynolds number Re_c of an elliptical foil by varying the flapping frequency and amplitude. Zhang *et al.,* [25] studied the effect of varying the thickness-to-chord ratio (δ) between 1 and 100 for elliptical and rectangular flapping foils on the symmetry-breaking bifurcation. Arora *et al.,* [18] studied the flow patterns, propulsion efficiency and power requirements associated with a heaving thin flat plate in a quiescent fluid. Deng and Caulfield [20] identified the onset of symmetry breaking around an elliptical foil by varying foil thickness to chord ratio ($\delta = e/D$, where *D* and *e* are chord length and thickness, respectively) in a viscous fluid subjected to a vertically forced oscillation Moreover, the flow field was assessed to be similar to the onset of asymmetry around a fixed cylinder. The nature of symmetry breaking was shown to depend on two non-dimensional parameters, namely Keulegan-Carpenter number (*KC*) and Stokes number (β) defined as

$$KC = \frac{2\pi A}{D}, \quad \beta = \frac{fD^2}{\nu} \tag{1}$$

where f is the plunging frequency and ν is the kinematic viscosity of the fluid [20]. In the case of a flow generated by a purely oscillating circular cylinder or elliptical foil, different patterns of asymmetry in $KC - \beta$ space have been reported [20,26]. These patterns are qualitatively different on either side of the marked 'freezing point', a term first proposed by Elston *et al.,* [26].

The identification of conditions leading to a tendency to propel for a plate of low δ at an apparent steady speed is extremely appealing in the context of our understanding of the flight of birds and insects. However, it is challenging to hold or capture the subtle equilibrium required to lead to a quasi-periodicity in the flow once a symmetry-breaking bifurcation is established. In such cases, it is difficult to accurately quantify the critical values of kinematic parameters that govern the onset of asymmetry in the flow. Further, the self-propulsion of rigid, flat, and low thickness to chord ratio $(\delta \le 1/10)$ plates has received limited attention. In addition, the effect of ground clearance on the growth or decay of perturbations has not been addressed before. The earlier studies mainly focused on types of asymmetries produced by oscillating circular cylinders and elliptical foil as a function of *KC*, *β,* and δ. Furthermore, the different types of asymmetries related to a self-propelled rigid plunging plate of low thickness to chord ratio need to be addressed. It has been reported that the onset of asymmetry or instability is not achieved even after a few hundred plunging cycles in some instances [18]. This augments uncertainty over the propulsion scenarios leading to a significant increase in the computational cost and time elapsed in accurate quantification of the point of transition from pure plunging to forward locomotion.

To address these limitations, we develop and present a framework to identify conditions under which symmetry breaking in the flow around a thin rigid rectangular plunging plate can be induced without having to rely on visual or trajectory-tracking techniques to isolate the eventual outcome. Going further, the present study has been conducted on a self-propelled rigid wing (the forward translation is produced only by a flapping motion and both are interdependent or linked) to mimic the action of a biological flyer. In the present investigation, the prediction of the onset of self-propulsion is performed using Floquet analysis by utilizing the periodic base flow produced by the plunging plate. The transition boundary in KC - β space between two-dimensional symmetrical and asymmetrical flow produced by a horizontally unconstrained rectangular plate plunging in a quiescent fluid for low thickness to chord ratios ($0.05 \le \delta \le 0.2$) is determined. Further, the trajectory of the rigid plate for kinematic conditions on the asymmetry side and near the transition boundary is analyzed. Finally, the role of ground clearance in inducing flow asymmetry leading to the propulsion of a plunging rectangular plate is investigated.

1.1 Problem Description

We consider a rigid rectangular plate unconstrained (or free to propel) in the direction transverse to the imposed plunging motion. A schematic illustrating the plunging plate is shown in Figure 1. For the non-dimensionalization of system parameters, chord *D* has been chosen as the length scale and flapping period *T* (where $T = f_0^{-1}$ f_0 is the plunging frequency) as the time scale. The vertical displacement of a rectangular plate is given by

$$y(t) = A\cos(2\pi f_o t) \tag{2}$$

The parameters expected to play a significant role in the propulsion of the plate and for conducting a parametric study are the flapping Reynolds number (Re_f), KC, β, δ, and ground clearance (ς). The flapping Reynolds number is defined as

$$Re_f = Af_o D/\nu = (KC \times \beta)/2\pi \tag{3}$$

The density ratio is defined as $\rho^* = \rho_s/\rho_f$, (where ρ_s is the density of the solid body and ρ_f is the fluid density). δ is varied between $0.05 \le \delta \le 0.2$ which is similar to that of a real insect wing [1,27,28]. The ground clearance $\varsigma = h/D$ is expressed as the non-dimensional distance of the plate from the bottom boundary of the domain (h). Such ground effect has not been studied earlier and can reveal how the distance from the ground can affect the self-propulsion of the plate. This is also analogous to an insect or a bird taking off from the ground by flapping its wings.

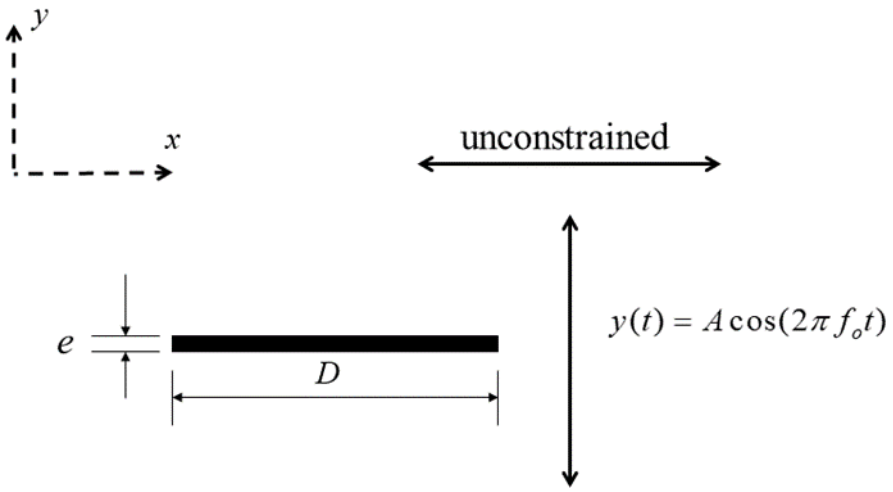

Fig. 1. Schematic representation of a self-propelled rigid plunging membrane

A hydrodynamic force is exerted on the flat plate due to its interaction with the fluid. The forward locomotion along the direction orthogonal to the plunging motion is made possible due to the horizontal component of this force. As the plate is unconstrained along the *x*-direction, the horizontal position of the plate x_p is updated by the numerical solution of Newton's second law of motion.

$$\bar{F}_x = m\frac{d^2x_p}{dt^2} \tag{4}$$

Here m is the mass of the plate and $\bar{F}_x$ is the instantaneous thrust exerted on it. The horizontal velocity component (u) is updated using the following rule

$$u = \frac{dx_p}{dt} \tag{5}$$

The thrust coefficient C_x is defined as $C_x = 2\bar{F}_x/\rho_f V^2 D$, where $V = 2\pi A f_0$ is the maximum plunging velocity.

In order to gain a comprehensive understanding of the dynamics related to the parameters of interest, it was considered necessary to select the range of design variables taking cognizance of previous research [17,20-25]. Therefore, the range of parameters has been chosen which is influenced by that of the smallest insect (e.g. *Encarsia Formosa* and *Drosophila melanogaster*) [1, 2] and given in Table 1. It should also be noted that the wings or fins of flying and swimming creatures have a density ratio $\rho^* \sim 10^1 - 10^2$ [22]. Hence in this work, the density ratio has been fixed at the mean value of 55.

Table 1
The scope of parameters (or configuration space) examined in this work for the parametric study of a rigid plunging plate

Variable	Minimum value	Maximum value
KC	1	8
β	1.7	95
δ	0.05	0.2
ς	2.0	10.0

2. Methodology

The present study encompasses two stages of numerical modeling: (a) flow solver, for calculation of the base flows around the plunging plate, (b) stability analysis, for the formulation of the eigenvalue problem. The base flow calculated through the flow solver is utilized for the stability analysis. The description of these approaches is given in the following sections.

2.1 Fluid Solver

The fluid solver utilizes the multi-relaxation time (MRT) version of the lattice Boltzmann method (LBM) to calculate the flow field and forces on the plunging plate. Details of the flow solver are given in Arora *et al.,* [18,29] and only the key aspects are presented here.

2.1.1 Multi-relaxation time LBM

The conventional single-relaxation time (SRT) LBM poses numerical instability at low values of relaxation time and hence presents limitations in modeling of flows at high Reynolds numbers [30-35]. Contrary to SRT, the MRT model exhibits better numerical stability even at high Reynolds numbers and has been quite successful in curtailing the spurious oscillations registered in force measurement [34,35]. In this method, the distribution function *f* (as defined in the SRT model) in the discrete velocity space B is mapped onto the moment space K by using a transformation matrix *M* [18], i.e., $\hat{f} = Mf$, where $\hat{f}$ is a column matrix consisting of hydrodynamic moments of the velocity distribution function (each row vector) that represent macroscopic variables, such as density, kinetic energy and its square, and the momentum flux viscous stress tensor in a two-dimensional space. The collision process is performed in the K space given as $\hat{f}_* = \hat{f} - S[\hat{f} - \hat{f}^{eq}]$, where $\hat{f}_*$ is the post-collision distribution and *S* is the diagonal relaxation time matrix

$$S = diag[s_1, s_2, s_3, s_4, s_5, s_6, s_7, s_8, s_9] \tag{6}$$

Where $s_1 = s_4 = s_6 = 0$ (relaxation time for the conserved quantities, i.e., mass and momentum flux). Thus, each relaxation time can be individually adjusted for different physical quantities in MRT which leads to its higher numerical stability than the BGK version. The MRT model reduces to the BGK model if all the diagonal terms are equal, i.e., $s = 1/\tau$ where τ is the single-relaxation time.

2.1.2 Moving boundary treatment

For a moving boundary [18,29,35,36] a set of boundary nodes at the midpoints of the links connecting the fluid and solid nodes are used to represent the solid surface (shown in Figure 2).

The distribution functions reflected from the solid surface back to the fluid nodes can be written as

$$f_{\bar{\alpha}}(\boldsymbol{x}_f, t + \Delta t) = \tilde{f}_{\alpha}(\boldsymbol{x}_f, t) + w_{\alpha}\rho\frac{6}{c^2}\mathbf{e}_{\bar{\alpha}} \cdot \mathbf{u}_b \tag{7}$$

The last term in Eq. (7) reflects the transfer of momentum between the fluid and the moving solid boundary [30]. Here $\mathbf{e}_{\bar{\alpha}} = -\mathbf{e}_{\alpha}$ and $\mathbf{u}_b$ is the velocity of the boundary node which is assumed to be situated precisely halfway along with the link between solid and fluid nodes.

$$\mathbf{u}_b = \mathbf{U} + \boldsymbol{\omega} \times \left(\mathbf{x}_f + \frac{1}{2}\mathbf{e}_{\alpha}\Delta t - \mathbf{X} \right) \tag{8}$$

Here $\mathbf{U}$ is the velocity of translation, $\boldsymbol{\omega}$ is the angular velocity and $\mathbf{X}$ is the position-vector of the center of mass of the solid.

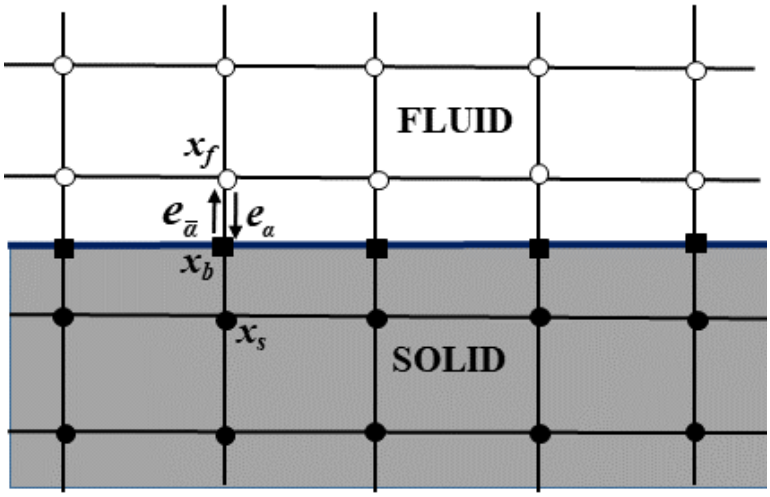

Fig. 2. The layout [37] of the regularly spaced lattices and the solid boundary (solid blue). The filled and hollow circles signify solid and fluid nodes individually. The solid squares denote the boundary nodes

In this technique, the lattice nodes are handled in the same fashion on either side of the boundary surface, i.e. the fluid fills the whole domain [30]. This change is utilized for reflecting the two incoming

post-collision distributions $\tilde{f}_\alpha(\mathbf{x},t)$ and $\tilde{f}_{\bar{\alpha}}(\mathbf{x}+\mathbf{e}_\alpha\Delta t,t)$ from the fluid and solid sides at each boundary node, relating to the velocities $\mathbf{e}_\alpha$ and $\mathbf{e}_{\bar{\alpha}}$ along the links connecting $\mathbf{x}_f$ and $\mathbf{x}_f+\mathbf{e}_\alpha\Delta t$. The two reflected distributions are updated by

$$f_\alpha\left(\mathbf{x}_f+\mathbf{e}_\alpha\Delta t,t+\Delta t\right)=\tilde{f}_{\bar{\alpha}}\left(\mathbf{x}_f+\mathbf{e}_\alpha\Delta t,t\right)+2w_\alpha\rho\frac{3}{c^2}\mathbf{e}_\alpha\cdot\mathbf{u}_b \tag{9}$$

$$f_{\bar{\alpha}}\left(\mathbf{x}_f,t+\Delta t\right)=\tilde{f}_\alpha\left(\mathbf{x}_f,t\right)-2w_\alpha\rho\frac{3}{c^2}\mathbf{e}_\alpha\cdot\mathbf{u}_b \tag{10}$$

This methodology ensures that mass is conserved at the boundary nodes and additionally prevents the need for creating and destroying fluid because of the movement of the solid objects.

2.2 Floquet Analysis

In this section, the formulation of the problem and the equations that govern the evolution of the disturbance are described. The numerical methods which are used for the formulation of the eigenvalue problem for the determination of critical state are outlined as well. In order to study the stability of the two-dimensional time-periodic base flow, a temporal Floquet stability analysis is used. The base flow is assumed to be time-periodic with period *T* such that $\mathbf{u}\left(x,y,t_0+T\right)=\mathbf{u}\left(x,y,t_0\right)$.

The non-dimensional form of the governing equations that describe the flow of an incompressible Newtonian fluid are,

$$\nabla\cdot\mathbf{u}=0 \tag{11}$$

$$\frac{\partial\mathbf{u}}{\partial t}+\mathbf{u}\cdot\nabla\mathbf{u}=-\nabla p+\frac{1}{Re_f}\nabla^2\mathbf{u} \tag{12}$$

where $\mathbf{u}$ is the velocity and p is the pressure. In two dimensions, the continuity and the momentum Eq. (11) and (12) are transformed to vorticity (ω) transport and stream function (ψ) form, given as

$$\nabla^2\psi=-\omega \tag{13}$$

$$\frac{\partial\omega}{\partial t}+\frac{\partial\psi}{\partial y}\frac{\partial\omega}{\partial x}-\frac{\partial\psi}{\partial x}\frac{\partial\omega}{\partial y}=\frac{1}{Re_f}\nabla^2\omega \tag{14}$$

To determine the flow stability at an arbitrary phase (i.e., t_0), the flow is decomposed into the base state or base flow $\left(\bar{\omega},\bar{\psi}\right)$, and an unsteady or perturbed part $\left(\omega',\psi'\right)$ by

$$\omega\left(x,y,t_o\right)=\bar{\omega}\left(x,y,t_o\right)+\varepsilon\omega'\left(x,y,t_o\right) \tag{15}$$

$$\psi\left(x,y,t_o\right)=\bar{\psi}\left(x,y,t_o\right)+\varepsilon\psi'\left(x,y,t_o\right) \tag{16}$$

where ε is a small parameter. Substituting into Eq. (13) and (14), subtracting the equations for the base flow and dropping higher-order terms, the following linearized perturbation equations can be obtained for the perturbed vorticity and stream function

$$\frac{\partial \omega'}{\partial t} + \frac{\partial \bar{\psi}}{\partial y}\frac{\partial \omega'}{\partial x} + \frac{\partial \psi'}{\partial y}\frac{\partial \bar{\omega}}{\partial x} - \frac{\partial \bar{\psi}}{\partial x}\frac{\partial \omega'}{\partial y} - \frac{\partial \psi'}{\partial x}\frac{\partial \bar{\omega}}{\partial y} = \frac{1}{Re_f}\nabla^2 \omega' \tag{17}$$

$$\nabla^2 \psi' = -\omega' \tag{18}$$

In this work, we represent the perturbed vorticity and stream function in terms of normal modes

$$\omega'(x,y,t_o) = \hat{\omega}\left(x,y,t_o\right)e^{-\sigma(t-t_o)} \tag{19}$$

$$\psi'(x,y,t_o) = \hat{\psi}\left(x,y,t_o\right)e^{-\sigma(t-t_o)} \tag{20}$$

Where $\hat{\omega}\left(x,y,t_0\right)$ and $\hat{\psi}\left(x,y,t_0\right)$ are *T*-periodic Floquet eigenvectors evaluated at arbitrary phase t_0 and σ is the Floquet exponent. The Floquet multiplier μ is associated to the Floquet exponent σ by $\mu = e^{-\sigma T}$. Generally, the exponents, the multipliers and the eigenfunctions can either be real or exist as complex-conjugate pairs. The instability is characterized by the multiplier leaving the unit circle (i.e., $|\mu| > 1$) or equivalently when the real part of a Floquet exponent becomes negative.

Substituting (19) and (20) into (17) and (18), an eigenvalue problem with the growth rate being the eigenvalue can be formulated as

$$\sigma\hat{\omega} = \frac{\partial \bar{\psi}}{\partial y}\frac{\partial \hat{\omega}}{\partial x} + \frac{\partial \hat{\psi}}{\partial y}\frac{\partial \bar{\omega}}{\partial x} - \frac{\partial \bar{\psi}}{\partial x}\frac{\partial \hat{\omega}}{\partial y} - \frac{\partial \hat{\psi}}{\partial x}\frac{\partial \bar{\omega}}{\partial y} - \frac{1}{Re}\left(\frac{\partial^2}{\partial x^2} + \frac{\partial^2}{\partial y^2}\right)\hat{\omega} \tag{21}$$

$$\hat{\omega} + \left(\frac{\partial^2}{\partial x^2} + \frac{\partial^2}{\partial y^2}\right)\hat{\psi} = 0 \tag{22}$$

For a structured and uniformly spaced grid, the discretized form of Eq. (21) and (22) can be written in a condensed matrix form as

$$\sigma\begin{pmatrix} 1 & 0 \\ 0 & 0 \end{pmatrix}\begin{pmatrix} \hat{\omega} \\ \hat{\psi} \end{pmatrix} = \begin{pmatrix} a_{11} & a_{12} \\ a_{21} & a_{22} \end{pmatrix}\begin{pmatrix} \hat{\omega} \\ \hat{\psi} \end{pmatrix} \tag{23}$$

where coefficients a_{11}, a_{12}, a_{21} and a_{22} are functions of the flow parameters governing the base flow. The coefficients of these linear equations are determined by computing the base flow whose stability is to be established. The eigenvalue problem represented by Eq. (23) yields a generalized matrix eigenvalue problem of the form

$$\mathbf{Jx} = \sigma\mathbf{Mx} \tag{24}$$

where **x** is an eigenvector that contains the unknown values of vorticity $\hat{\omega}$ and stream function $\hat{\psi}$. It can be seen from Eq. (23) that the mass matrix **M** is singular, symmetrical and real, while the Jacobian matrix **J** is asymmetrical and real. Eq. (24) is solved by inverting the eigenvalue problem to a form that does away with the singularity of the mass matrix. Thus, the system is written as

$$\mathbf{Bx} = \eta \mathbf{x} \tag{25}$$

where $\mathbf{B} = \mathbf{J}^{-1}\mathbf{M}$ and $\eta = 1/\sigma$.

The size of the Jacobian and mass matrices depends on the number of perturbed parts (ω', ψ'). For implementing and forming the discretized problem into the eigenvalue problem of the type given by (25), the vector storage of the perturbed space of the solution is required. A variable is introduced that stores the global count of all grid points that are spanned in the discretized domain. The global counts are assigned sequentially, starting from one side of the boundary and traversing every point. This variable maps the compass notation of the grid to the vector storage location. In this way, the Jacobian matrix with defined locations for the constituting elements in the matrix is obtained by a pre-defined global count of the respective grid point. The method of assigning the Jacobian matrix for the grid points is depicted in Figure 3 and Table 2. To formulate the eigenvalue problem given by (25), the partial differential equations are discretized on a uniform grid using the finite-difference method. Fourth-order central differences are used for all the interior nodes, while forward or backward differences of second-order accuracy are used at the boundaries. The Krylov subspace method is used for calculating the critical eigenvalues and respective eigenvectors of **B**.

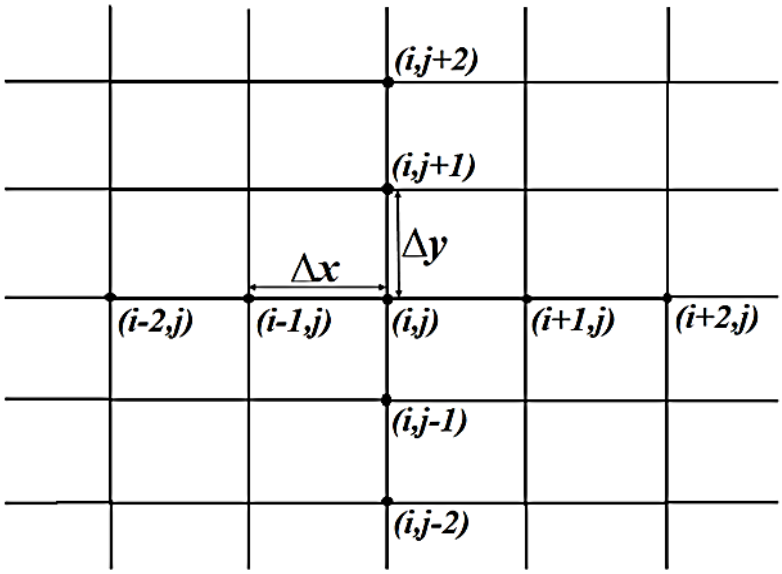

Fig. 3. Typical grid spacing diagram and the nomenclature for the distances used

Table 2
Global count representation of the points on the grid for a fourth order discretization of terms in Eq. (21) and (22)

Gridpoint	Global count	Storage location for $\hat{\omega}$	Storage location for $\hat{\psi}$
i,j	m	2m-1	2m
i-1,j	m_1	$2m_1$-1	$2m_1$
i,j-1	m_2	$2m_2$-1	$2m_2$
i+1,j	m_3	$2m_3$-1	$2m_3$
i,j+1	m_4	$2m_4$-1	$2m_4$
i-2,j	m_5	$2m_5$-1	$2m_5$
i,j-2	m_6	$2m_6$-1	$2m_6$
i+2,j	m_7	$2m_7$-1	$2m_7$
i,j+2	m_8	$2m_8$-1	$2m_8$

2.3 Computational Domain

The layout of the computational domain is shown in Figure 4. The size of the computational domain was 20*D*×20*D*, where *D* is the length (or chord) of the plunging plate. The edges of the plate were positioned 9.5*D* from both the left and right faces of the domain. No-slip boundary condition (zero fluid velocity) was enforced on the top and bottom boundaries of the domain. The fluid was taken to be stagnant initially. Outflow boundary conditions were imposed on both the far-faces (upstream and downstream) of the domain as given by Aidun *et al.,* [38].

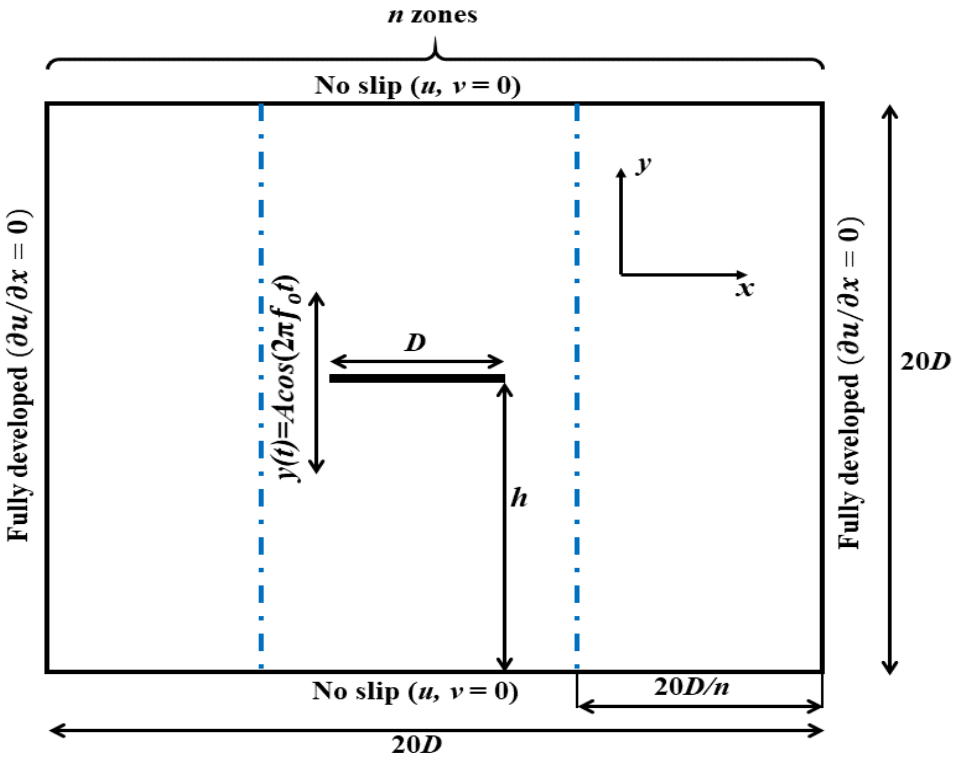

Fig. 4. Layout of the computational domain with imposed boundary conditions separated into various zones (by blue dash-dot lines) assigned to each processor

To take advantage of the use of LBM, the solver was parallelized using a message passing interface (MPI) in which the domain along the *x*-direction was sliced into *n* sub-zones, where *n* is the number

of processors. In this manner, every processor was allocated a sub-domain with $(20/n)D \times 20D$ physical size.

Simulations for a symmetric elliptical airfoil at various *KC* and β were performed to validate the fluid solver. The translational boundary that allowed horizontal motion was compared against published results [20]. The density ratio ρ^* and δ of the elliptical membrane were taken as 10 and 0.1, respectively, as reported in their work [20]. The outcomes obtained (shown in Figure 5) show an excellent agreement of the present numerical model with those of Deng and Caulfield [20]. Moreover, the symmetrical and asymmetrical flow patterns are represented by the left and right areas of the curved line in Figure 5.

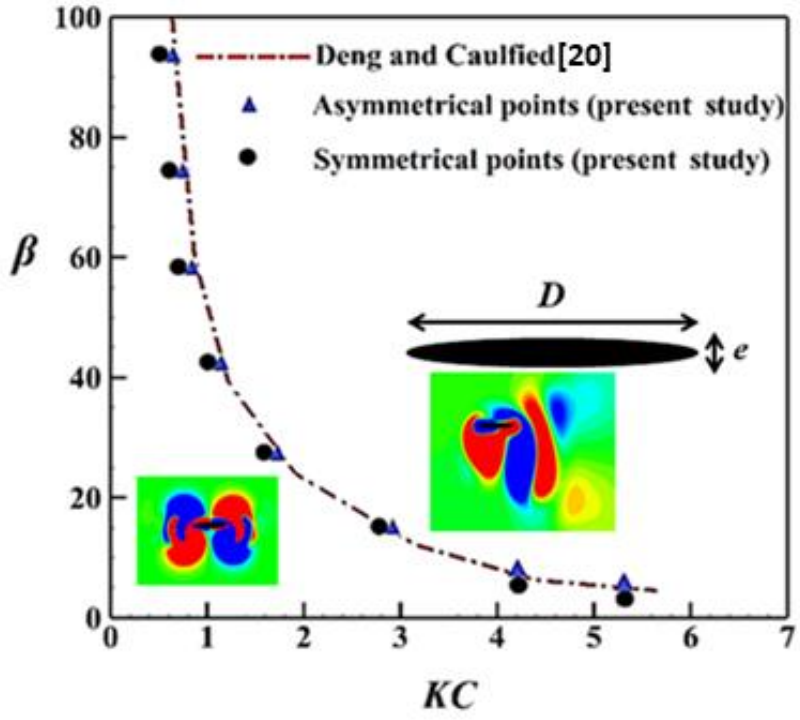

Fig. 5. The geometry of an elliptical foil with (δ=0.1) and comparison of the location of transition boundaries in KC-β space between the two-dimensional symmetrical and asymmetrical flow of the present study with Deng and Caulfied [20]

3. Results and Discussion

In this section, results obtained for various *KC*, β and δ through numerical simulations and Floquet analysis for an unconstrained plunging thin two-dimensional rectangular plate are presented and discussed.

3.1 Symmetric Flow

While the focus of this work is to predict the onset of propulsion of plunging plate in quiescent fluid, it is equally important to look at a symmetric flow scenario as well. We consider the dynamics of the rectangular plate plunging for *KC* = 3.8 and β = 1.7 as shown in Figure 6. The simulation was conducted for 60 plunging cycles at the end of which no instability or instigation of propulsion was

noticed. For these conditions, the upstroke begins (as shown in Figure 6(a)) with vortices forming at both the edges and develop until the midstroke (as shown in Figure 6(b)). As the plate reaches the beginning of the downstroke, the vortices formed during the upstroke on either edge are quickly dissipated and a new inverse pair of vortices is formed (as shown in Figure 6(c)). The vortices experience viscous dissipation and maintain symmetry during each stroke. As a result, there is no plate-wake interaction and the asymmetry that could have pushed the plate into forwarding motion is not realized. A similar formation and dissipation of vortices occurs during the downstroke. The state was found to be stable to an initial perturbation, in the form of a small momentum, which also failed to grow even after the plate finished the previously mentioned plunging strokes.

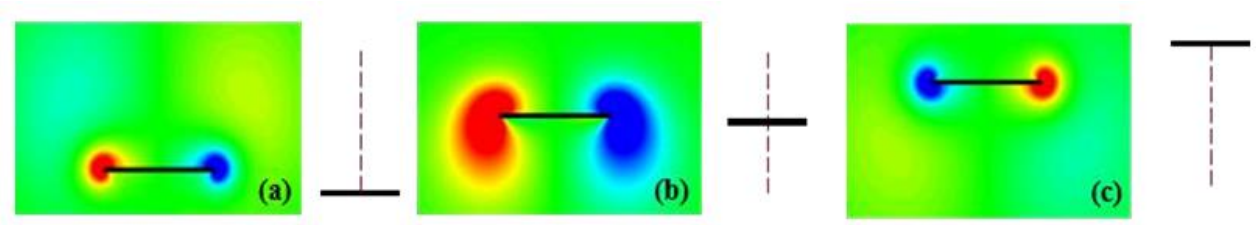

Fig. 6. Contours of non-dimensional vorticity field produced due to the plunging motion of the rectangular plate at *KC* = 3.8 and β = 1.7. The accompanying figure on the right illustrates the instantaneous position and the direction of motion during one stroke. Blue and red colors demonstrate clockwise and anticlockwise rotations, respectively (between -0.30 (blue) and +0.30 (red))

3.2 Symmetry Breaking

Results of numerical simulations performed when the plate attains self-propelled motion for various values of δ $\left(0.05 \le \delta \le 0.2\right)$ are presented here. We also identify a transition boundary that separates symmetrical and asymmetrical flow patterns and allows horizontal motion in *KC*-β space. After conducting a series of simulations with a large number of *KC* and β pairs, the transition region was identified between symmetrical and asymmetric flow associated with the plunging rigid plate in *KC*-β space for three different δ. The transition region between the curves is narrower when β is small and *KC* is large. On the other hand, this region becomes significantly wider for large β and small *KC*.

The general form of the empirical relations that have been obtained after regression fitting for critical Stokes number (β_c) and Reynolds number (Re_{fc}) for δ = 0.05, 0.1 and 0.2 for $1 \le KC \le 8$ are,

$$\beta_c = a_0 KC^{-a_1} \tag{26}$$

$$Re_{fc} = \left(\frac{\beta_c KC}{2\pi}\right) = b_0 KC^{-b_1} \tag{27}$$

Here a_0, a_1, b_0, and b_1 are the coefficients, whose values depend on δ and are given in Table 3. Such reduced-order relationships are expected to be of great utility for designers using the same kinematic concept for flapping wing flyers.

Table 3
Values of a_0, a_1, b_0, and b_1 for varying δ corresponding to the Eq. (26) and (27)

δ	a_0	a_1	b_0	b_1
0.05	93.9	1.67	14.5	0.67
0.1	93.1	1.63	14.8	0.63
0.2	202.55	1.88	32.24	0.88

3.3 Floquet Analysis

Figure 7 shows the curves of marginal stability for $\delta = 0.1$ in *KC*-β and *KC*-Re_f space. These curves separate symmetrical and asymmetrical flow patterns (for a horizontally unconstrained plunging plate) under and over the curve, respectively. These curves provide valuable information on the onset of propulsion of the plunging plate for a particular value of *KC* and given values of β and Re_f.

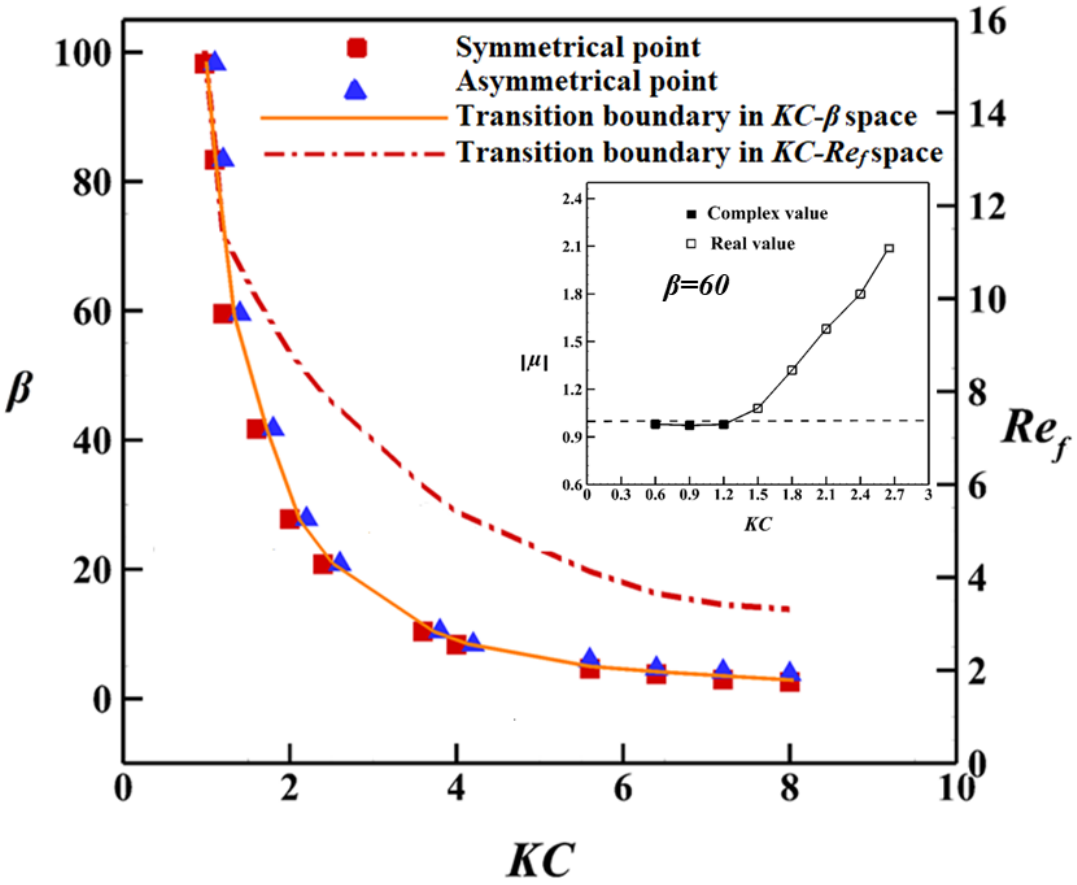

Fig. 7. Variation of flow transition boundaries characterizing conditions for horizontal motion in *KC*-β and *KC*-Re_f space for δ =0.1. The inset displays the variation of Floquet multiplier with *KC* for β =60

The curve is steeper for low *KC* and high β ($\beta \geq 40$) and hence a small variation in *KC* leads to a large change in β_c. The two-dimensional Floquet multiplier $\left(|\mu|\right)$ for $\beta = 60$ as a function of *KC* is shown in the inset. The Floquet analysis results show that the Floquet multipliers occur in complex-conjugate pairs for $KC \leq 1.2$ and have a magnitude less than one $\left(|\mu| < 1\right)$, while for $KC \geq 1.5$ the first Floquet multiplier crosses the unit circle with a single real value and magnitude greater than one

$(|\mu| > 1)$. These results show that the critical value of *KC* for the onset of asymmetry or instability is in the range of 1.2-1.5. This is further confirmed by direct numerical simulations of the plunging plate as shown in Figure 8. The non-dimensionalized coordinate (*X*) of the center of mass of the self-propelled plunging plate as a function of time (*t/T*) for $\beta = 60$ and $KC = 1.2$ shows that the displacement of the plate on either side of the initial position is negligible. This provides further verification that the plunging plate is in stable equilibrium for $KC = 1.2$. However, instability is clearly exhibited at $KC = 1.5$, where the coordinate of the center of mass of the plate appears to oscillate with time.

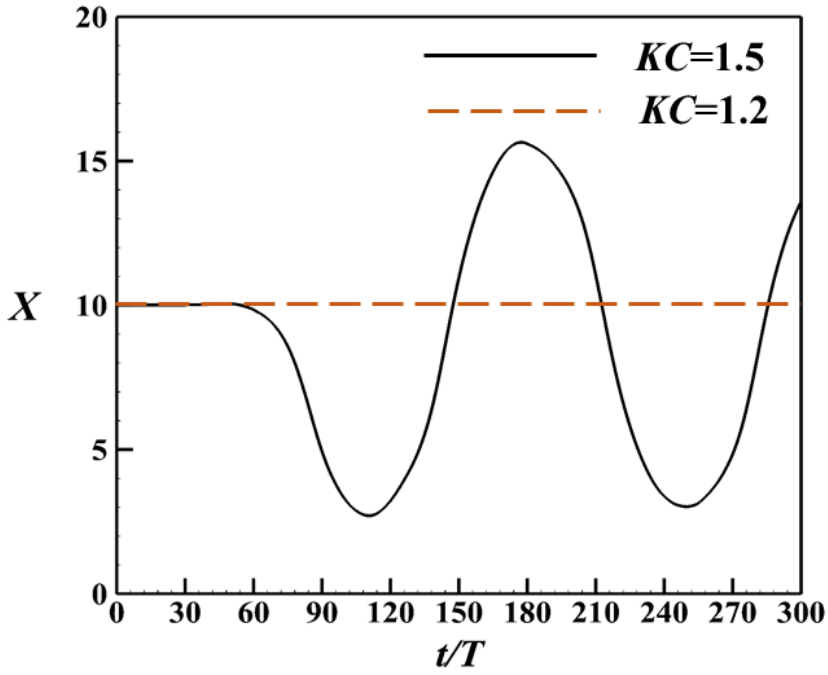

Fig. 8. A comparison of the non-dimensionalized trajectory coordinate (*X*) of the centre of mass of the self-propelled plunging plate as a function of plunging cycles (*t/T*) for *KC*= 1.2 and *KC*= 1.5

In addition, the vorticity contours of the periodic base flow calculated for the preliminary plunging cycles with $\delta = 0.1$ and $\beta = 60$ at $KC = 1.2$ and $KC = 1.5$ are shown in Figure 9(a) and 9(c), respectively. These flow patterns are shown for at *t/T*=5, at the instant when the plunging plate was at its maximum displacement in the *y*-direction. Figures 9(b) and 9(d) show the vorticity contours of a Floquet eigenfunction calculated from the base flows. The Floquet eigenfunction in Figure 9(b) shows symmetry about a line passing through the center of the plate. On the other hand, and as shown in Figure 9(d), this symmetry breaks for $\beta = 60$ and $KC = 1.5$ due to the Floquet multiplier crossing the unit circle. Observing the base flows shown in Figures 9(a) and 9(c), it is clearly not visually possible to identify whether each system is stable or not. However, the calculation of the Floquet eigenfunction and Floquet multiplier makes it possible to comment on the stability characteristics of the time-varying base flow. Therefore, our work demonstrates the prediction of instability (or onset of propulsion) using data from preliminary plunging cycles itself.

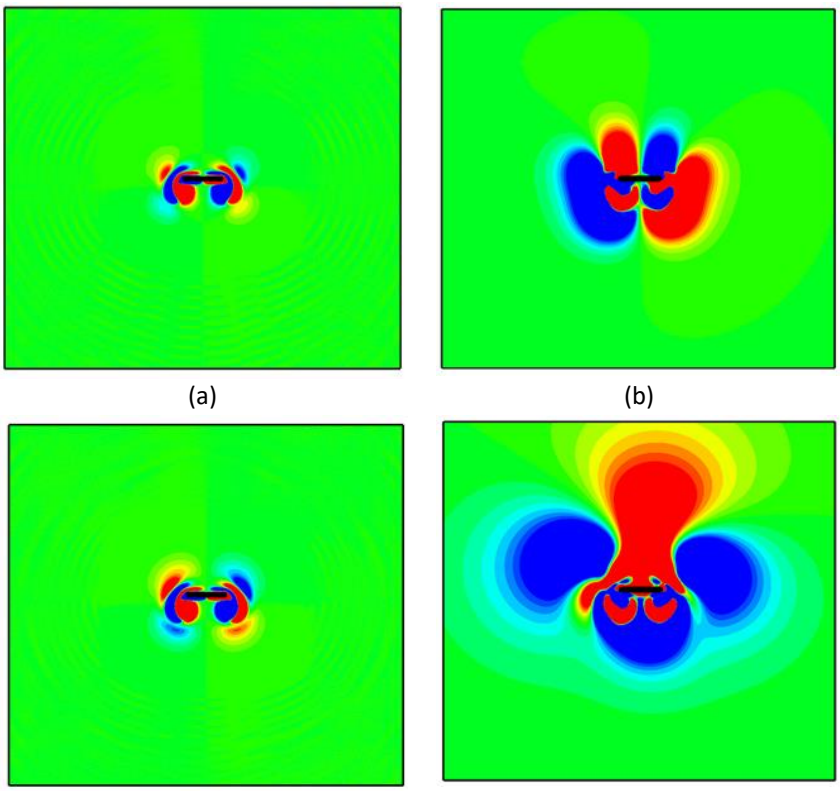

Fig. 9. The non-dimensionalized vorticity contours in the range -0.40 (blue) and +0.40 (red) for $\beta = 60$ for δ =0.1. (a) Base flow at *KC*=1.2. (b) Eigenvector at *KC*=1.2. (c) Base flow at *KC*=1.5. (d) Eigenvector at *KC*=1.5

3.4 Horizontal Movement in the Transition Regime

In this section, we describe different scenarios pertaining to a thin plunging plate (δ=0.05) in the transition regime and about to achieve propulsion. These movements are shown in Figure 10(a) corresponding to cases marked as (1) *KC*=1.2 and β=83.3, (2) *KC*=1.8 and β=41.7, (3) *KC*=2.4 and β =20.8 and (4) *KC*=4.2 and β=8.3 in Figure 10(b). The insets of Figure 10(a) show the non-dimensionalized trajectory coordinate (*X*) as a function of plunging cycles for the four scenarios that have been chosen due to the very distinct horizontal movements of the plates in these cases. For (1) and (2), the plate propels continuously in the negative *X*-direction. However, the plate in (1) leads (2) in propulsion, while in (3) it moves back and forth about the initial position with an amplitude that increases with time. In (4), the plate oscillates with a lower but fixed amplitude. The reasons for the different horizontal movements of the plunging plate, as described in these four cases can be understood by scrutiny of flow patterns and force histories. Figure 11 shows the wake structures for the four cases. The time-varying thrust coefficient (C_x) and phase portraits of these thrust coefficients are also shown in Figures 12(a) and 12(b), respectively. As can be observed for case (1) in Figure 11, the anti-clockwise rotation TEV attached to the plate at the mid-instant of the downstroke is able to navigate and make a strong vortex dipole at the trailing edge due to the combined influence of low plunging amplitude and high plunging frequency. These opposite rotation vortices at the trailing edge create a pressure imbalance along the chordwise direction. This pressure differential reflects in the form of a relatively large thrust in (1), as is indicated in the force coefficient shown in Figure 12(a). Thus, a higher thrust results in an earlier initiation of propulsion. For the other

cases (i.e., (2), (3) and (4)), the anti-clockwise rotation TEV is detached before the middle of the downstroke, making a weak vortex dipole at the trailing edge. The vortex dipole street at the trailing edge generates a reaction force in the opposite direction, manifesting as thrust [16,36].

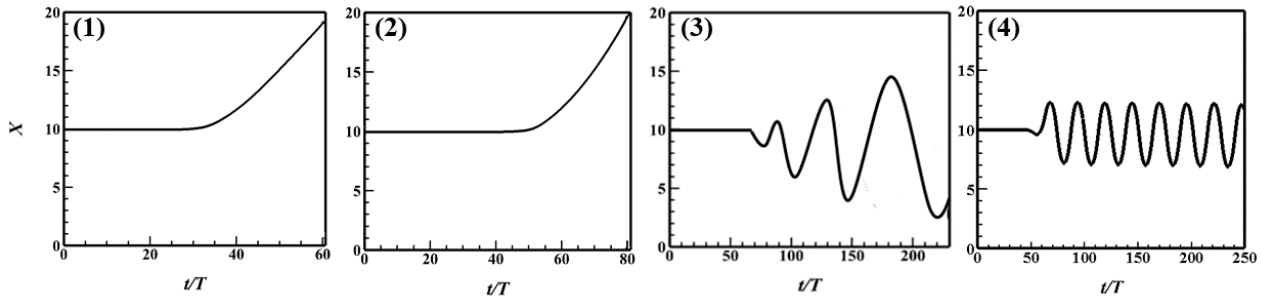

(a)

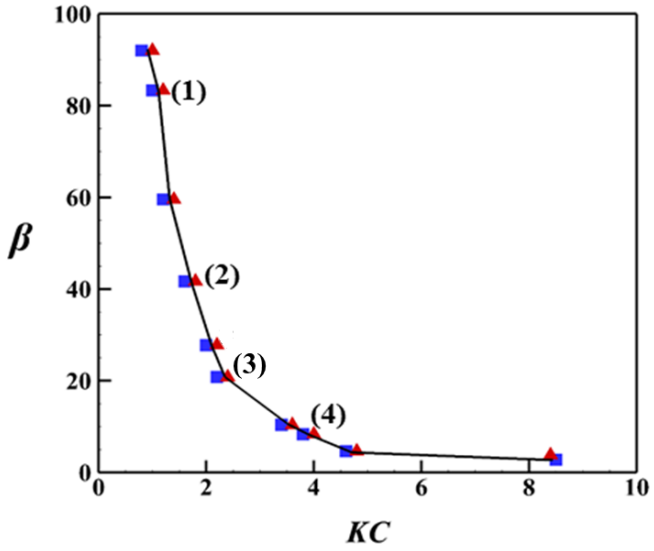

(b)

Fig. 10. (a) Variation in the non-dimensional trajectory coordinate (X) for δ=0.05 of center of mass at (1) KC=1.2 and β=83.3, (2) KC=1.8 and β=41.7, (3) KC=2.4 and β=20.8 and (4) KC=4.2 and β=8.3 with plunging cycles. (b) Location of transition boundary as a function of KC-β with cases marked as (1), (2), (3) and (4)

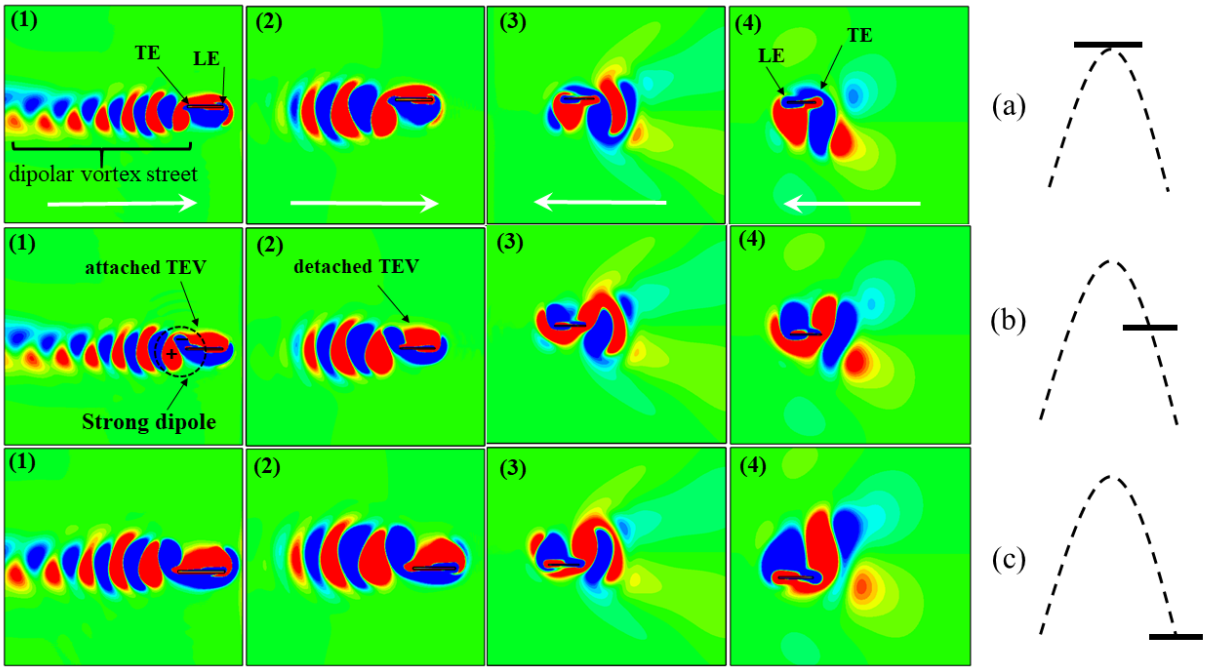

Fig. 11. Wake patterns associated with plunging flat plate for cases (1), (2), (3) and (4). The right column ((a,b,c)) shows the instantaneous positions during the cycle. Red and blue colors indicate anti-clockwise and clockwise rotation respectively. The white arrows show the direction of the horizontal movement of the plate

It is clear from Figure 11 that the vortex dipole street at the trailing edge is longest for (1) and gradually decreases down to (4). Due to these reasons, the magnitude of the thrust coefficient also decreases from (1) to (3) but unexpectedly increases in (4) as shown in Figure 12(a). In order to explain this, the phase portrait showing the variation of dC_x/dt against C_x for all four cases has been shown in Figure 12(b). It can be observed that the magnitude of dC_x/dt progressively decreases from (1) to (4). Hence, despite the higher value of C_x in (4), the plate oscillates around its mean position due to the largest timescale of periodicity of C_x. This behavior of forces due to wing-wake interaction decides the horizontal movement of the plunging plate.

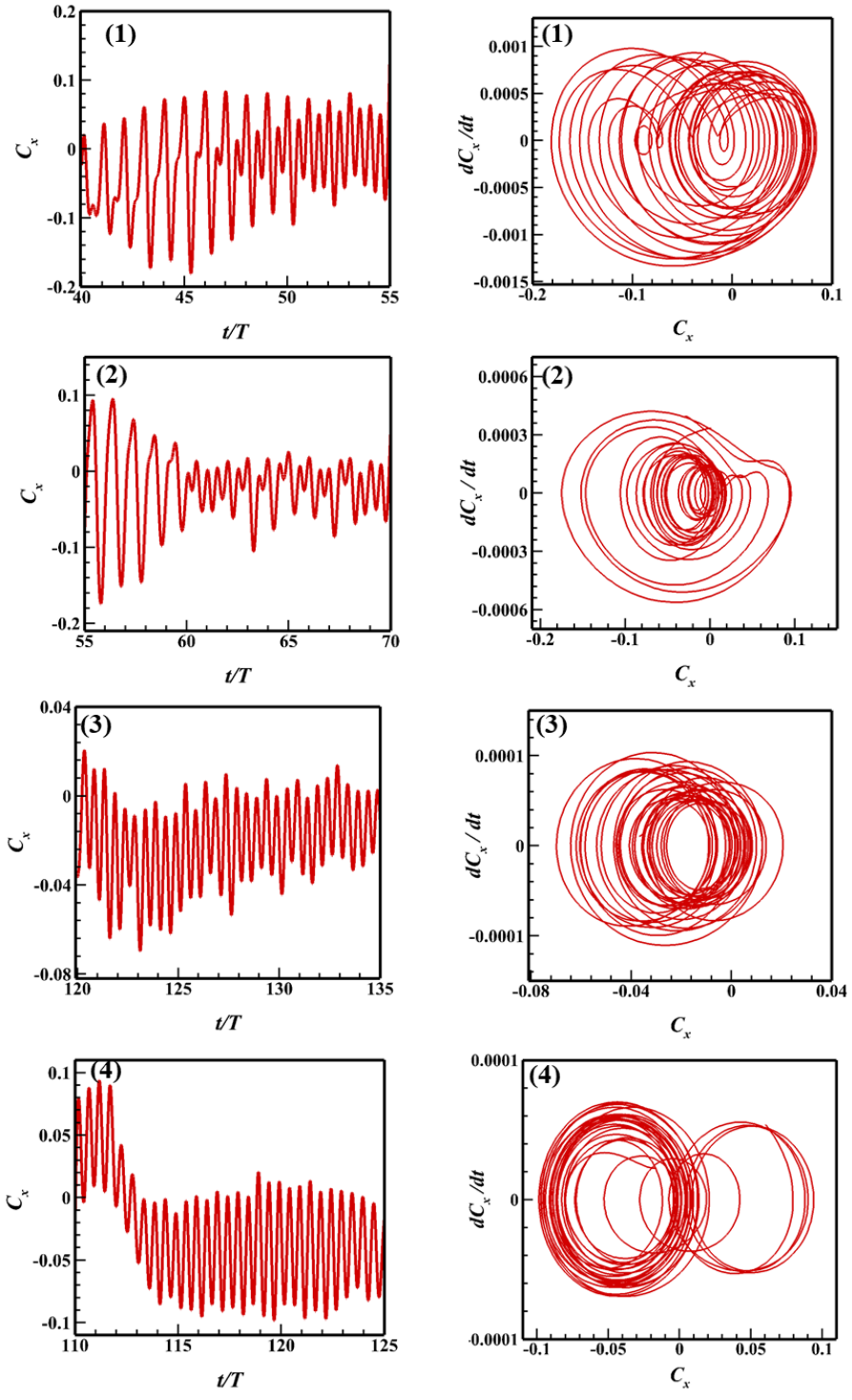

Fig. 12. (a) Time variation of horizontal thrust for cases (1), (2), (3), and (4). (b) Phase portraits plotting the time rate of change dC_x/dt of the horizontal thrust against C_x for the same cases (i.e. (1), (2), (3), and (4))

3.5 Effect of Ground Clearance (ς) on Symmetry Breaking

The effect of ground clearance (ς) on the propulsion of the plunging rigid rectangular plate for $\delta = 0.05$ with $KC = 1.8$ and $\beta = 41.7$ is shown in Figure 13. There is a small difference and a phase lag is observed between the propulsion at ς =10 and ς =6, while propulsion appears to be lagging behind significantly for ς =2 and occurs in the opposite direction. This lag in propulsion is further investigated by examination of the circulation (Γ) around the plate at $t/T = 30$. This choice was motivated by the fact that the rigid plate did not exhibit horizontal locomotion in any of the three scenarios at this instant of time.

The magnitude of velocity induced by the vortex dipole associated with the plate is given as

$$U_{dipole} = \frac{\Gamma}{2\pi\xi} \tag{28}$$

where ξ is the separation between the vortex centers of the dipole [7]. This induced value of velocity symbolizes the downwash and characterizes the magnitude of the thrust produced by the plunging motion of the plate. Γ has been determined by integrating the vorticity over a rectangular box of size $4D \times 3D$ considered around the plate as shown in Figure 14(a).

The circulation calculated for the three cases (i.e., ς =2, ς =6 and ς =10) is shown in Figure 14(b). It can be observed that the circulation increases on increasing the ground clearance. Figure 14(b) also shows that the circulation around the plunging plate is maximum for ς = 10 and minimum for ς = 2. This indicates that the plate farthest from the ground leads in propulsion rather than the plate nearest to it. Therefore, one may correlate this with biological flight and expect that insects and birds perched on an elevated structure (e.g., tree branches) can propel more quickly than insects and birds resting on the ground.

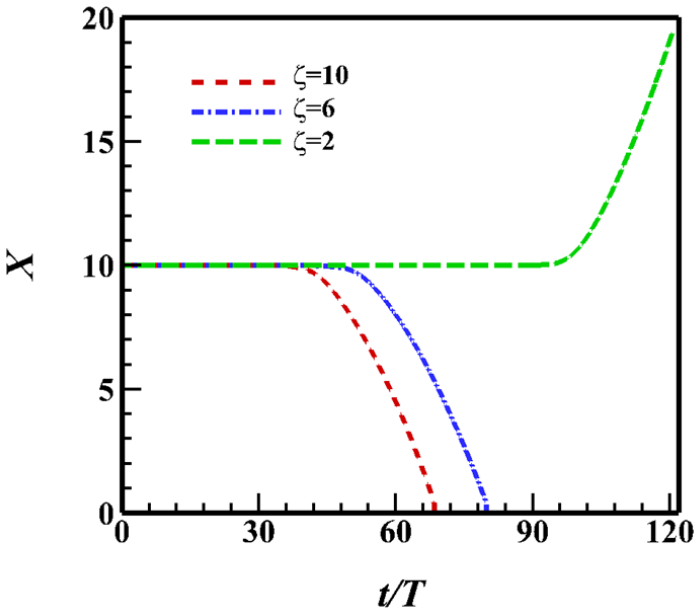

Fig. 13. The non-dimensional trajectory coordinate (*X*) of the center of mass of self-propelled plunging plate as a function of flapping cycles for δ=0.05 at *KC*=1.8 and β =41.7 with different ground clearances

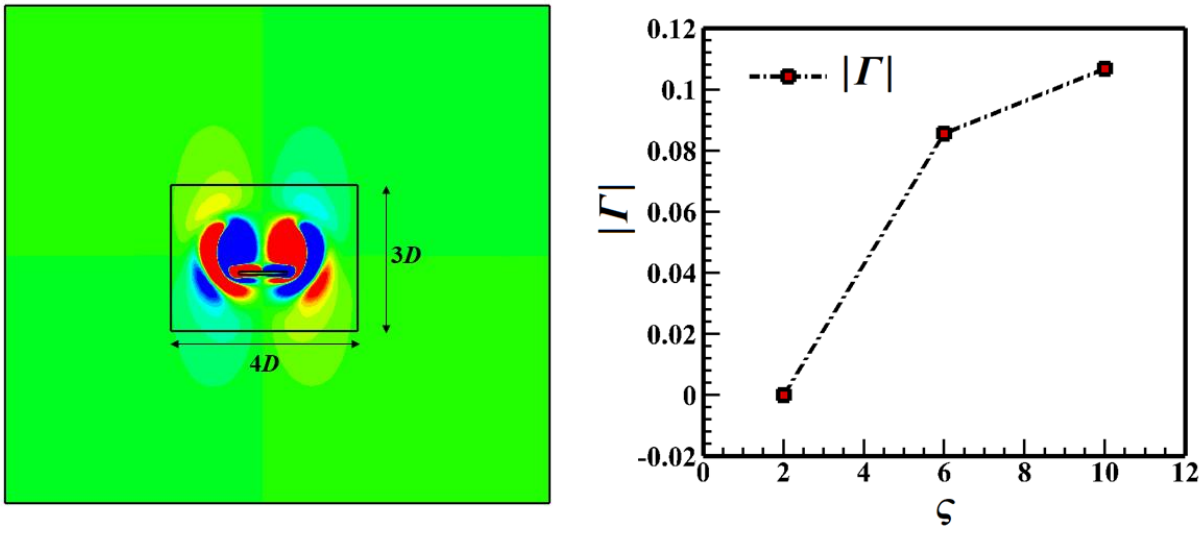

(a) (g)

Fig. 14. (a) A schematic representation of rectangular boxes ($4D \times 3D$) around the plate for calculating the circulation. (b) The variation of non-dimensional circulation ($|\Gamma|$) as a function of ground clearance (ς) with δ=0.05 at *KC*=1.8 and β =41.7 at *t/T*=30, when the instantaneous position at maximum displacement during the upstroke

4. Conclusions

This present work was directed towards the formulation and development of a linear stability analysis framework to numerically examine the self-propulsion of a rigid plunging plate in a quiescent fluid for different thickness to chord ratios δ $\left(0.05 \le \delta \le 0.2\right)$. To mimic a plunging rectangular rigid plate in a quiescent fluid, a fluid solver based on a multi-relaxation time version of the lattice Boltzmann method was used.

The stability of the periodic base flow around the plunging plate was analyzed through a time-saving Floquet analysis. In this regard, a two-dimensional discrete stability analysis framework (based upon the finite-difference method) was developed. Before the Floquet analysis, extensive work involved the study of a self-propelled rigid rectangular plate. A parametric investigation was performed to distinguish the influence of the Keulegan-Carpenter number (*KC*), Stokes number (β) and thickness-to-chord ratio (δ) on the onset of the population of the rectangular plate. It is vital to note that we have focused on parameter choices which are very close to the transition boundary, where our two-dimensional evaluation is most relevant. The *KC* - β curves indicated that the transition boundary shifted towards smaller *KC* for given β as δ was reduced, suggesting that breaking of symmetry was motivated for a plate with a lower thickness to chord ratio. The Floquet analysis of the periodic base flow generated by the plunging plate in *KC* - β space shows that the critical Floquet multiplier (μ_c) exists in complex conjugate pairs on the left of the transition boundary, while it becomes real on the right. This indicates symmetrical and asymmetrical flow patterns on the left and right sides of the transition boundary, respectively. The Floquet analysis was thus helpful in predicting, within a few initial strokes itself, whether a plunging plate will propel or not, greatly reducing computational cost and time in making an accurate prediction. As presented, if the magnitude of the Floquet multipliers is less than unity and the eigenvectors have a symmetry then there is no translation. On the other hand, the flow asymmetry transpired when the Floquet

multiplier exceeds unity, accompanied by the breaking down of corresponding eigenvector symmetry.

It was revealed that the plate shows four distinct trajectories on the asymmetry side and in the proximity of the transition boundary in *KC*-β space. These distinct movements were further differentiated from each other through the flow patterns associated with the plunging plate during propulsion. The non-dimensional coordinate of the center of mass (as a function of plunging cycles (*t/T*)) was shown to decrease from its mean value on moving towards the higher *KC* and lower β zone. The thrust coefficient (C_x) and its frequency ($\propto dC_x/dt$) were further utilized to understand these four different trajectories of the plate. It was revealed that a higher frequency of thrust coefficient instigated continuous linear movement in one direction, while the oscillating movement about a mean position is due to a lower frequency of the force coefficient. Finally, the ground clearance (ς) effect clearly shows that the plate which was farthest from the ground leads in propulsion as compared to a plate in its proximity. It is anticipated that this analysis will provide guidance for the onset of propulsion that can be attained for a given *KC* and β will be of significance in the design of systems with similar concepts.

Acknowledgement
N.K. acknowledges the financial support received from the Technical Education Quality Improvement Programme (TEQIP-III) of Uttarakhand Technical University, Dehradun. The authors also thank the IIT Delhi HPC facility for computational resources and Prof. Nadeem Hasan for insightful discussions.

References

[1] Shyy, Wei, Hikaru Aono, Chang-kwon Kang, and Hao Liu. *An introduction to flapping wing aerodynamics*. Vol. 37. Cambridge University Press, 2013. https://doi.org/10.1017/CBO9781139583916
[2] Shyy, Wei, Hikaru Aono, Satish Kumar Chimakurthi, Pat Trizila, C-K. Kang, Carlos ES Cesnik, and Hao Liu. "Recent progress in flapping wing aerodynamics and aeroelasticity." *Progress in Aerospace Sciences* 46, no. 7 (2010): 284-327. https://doi.org/10.1016/j.paerosci.2010.01.001
[3] Shyy, Wei, Yongsheng Lian, Jian Tang, Dragos Viieru, and Hao Liu. *Aerodynamics of low Reynolds number flyers*. 2008. https://doi.org/10.1017/CBO9780511551154
[4] Vogel, Steven. *Life in moving fluids: the physical biology of flow*. Princeton university press, 1996.
[5] Mueller, Thomas J. *Fixed and flapping wing aerodynamics for micro air vehicle applications*. AIAA, 2001. https://doi.org/10.2514/4.866654
[6] Ansari, S. A., R. Żbikowski, and Kevin Knowles. "Aerodynamic modelling of insect-like flapping flight for micro air vehicles." *Progress in aerospace sciences* 42, no. 2 (2006): 129-172. https://doi.org/10.1016/j.paerosci.2006.07.001
[7] Zhu, Xiaojue, Guowei He, and Xing Zhang. "How flexibility affects the wake symmetry properties of a self-propelled plunging foil." *Journal of fluid mechanics* 751 (2014): 164-183. https://doi.org/10.1017/jfm.2014.310
[8] Tsai, Bor-Jang, and Yu-Chun Fu. "Design and aerodynamic analysis of a flapping-wing micro aerial vehicle." *Aerospace Science and Technology* 13, no. 7 (2009): 383-392. https://doi.org/10.1016/j.ast.2009.07.007
[9] Knoller, Richard. "Die gesetzedes luftwiderstandes." *Flug-und Motortechnik (Wien)* 3, no. 21 (1909): 1-7.
[10] Katzmayr, Richard. *Effect of periodic changes of angle of attack on behavior of airfoils*. No. NACA-TM-147. 1922.
[11] Freymuth, Peter. "Propulsive vortical signature of plunging and pitching airfoils." *AIAA journal* 26, no. 7 (1988): 881-883. https://doi.org/10.2514/3.9982
[12] Freymuth, Peter. "Thrust generation by an airfoil in hover modes." *Experiments in Fluids* 9, no. 1 (1990): 17-24. https://doi.org/10.1007/BF00575331
[13] Triantafyllou, M. S., G. S. Triantafyllou, and R. Gopalkrishnan. "Wake mechanics for thrust generation in oscillating foils." *Physics of Fluids A Fluid Dynamics* 3, no. 12 (1991): 2835. https://doi.org/10.1063/1.858173
[14] Anderson, Jamie M., K. Streitlien, D. S. Barrett, and Michael S. Triantafyllou. "Oscillating foils of high propulsive efficiency." *Journal of Fluid mechanics* 360 (1998): 41-72. https://doi.org/10.1017/S0022112097008392
[15] Jones, K. D., C. M. Dohring, and M. F. Platzer. "Experimental and computational investigation of the Knoller-Betz effect." *AIAA journal* 36, no. 7 (1998): 1240-1246. https://doi.org/10.2514/2.505

[16] Lai, Joseph CS, and Max F. Platzer. "Characteristics of a plunging airfoil at zero freestream velocity." *AIAA journal* 39, no. 3 (2001): 531-534. https://doi.org/10.2514/2.1340
[17] Alben, Silas, and Michael Shelley. "Coherent locomotion as an attracting state for a free flapping body." *Proceedings of the National Academy of Sciences* 102, no. 32 (2005): 11163-11166. https://doi.org/10.1073/pnas.0505064102
[18] Arora, Nipun, Amit Gupta, Sanjeev Sanghi, Hikaru Aono, and Wei Shyy. "Flow patterns and efficiency-power characteristics of a self-propelled, heaving rigid flat plate." *Journal of Fluids and Structures* 66 (2016): 517-542. https://doi.org/10.1016/j.jfluidstructs.2016.08.005
[19] Benkherouf, T., M. Mekadem, H. Oualli, S. Hanchi, L. Keirsbulck, and L. Labraga. "Efficiency of an auto-propelled flapping airfoil." *Journal of Fluids and Structures* 27, no. 4 (2011): 552-566. https://doi.org/10.1016/j.jfluidstructs.2011.03.004
[20] Deng, Jian, and Colm-cille Patrick Caulfield. "Dependence on aspect ratio of symmetry breaking for oscillating foils: implications for flapping flight." *Journal of Fluid Mechanics* 787 (2016): 16-49. https://doi.org/10.1017/jfm.2015.661
[21] Hu, Jianxin, and Qing Xiao. "Three-dimensional effects on the translational locomotion of a passive heaving wing." *Journal of Fluids and Structures* 46 (2014): 77-88. https://doi.org/10.1016/j.jfluidstructs.2013.12.012
[22] Lu, Xi-Yun, and Qin Liao. "Dynamic responses of a two-dimensional flapping foil motion." *Physics of Fluids* 18, no. 9 (2006). https://doi.org/10.1063/1.2357733
[23] Vandenberghe, Nicolas, Stephen Childress, and Jun Zhang. "On unidirectional flight of a free flapping wing." *Physics of Fluids* 18, no. 1 (2006). https://doi.org/10.1063/1.2148989
[24] Vandenberghe, Nicolas, Jun Zhang, and Stephen Childress. "Symmetry breaking leads to forward flapping flight." *Journal of Fluid Mechanics* 506 (2004): 147-155. https://doi.org/10.1017/S0022112004008468
[25] Zhang, Xing, Saizhen Ni, Shizhao Wang, and Guowei He. "Effects of geometric shape on the hydrodynamics of a self-propelled flapping foil." *Physics of Fluids* 21, no. 10 (2009). https://doi.org/10.1063/1.3251045
[26] Elston, John R., Hugh M. Blackburn, and John Sheridan. "The primary and secondary instabilities of flow generated by an oscillating circular cylinder." *Journal of Fluid Mechanics* 550 (2006): 359-389. https://doi.org/10.1017/S0022112005008372
[27] Ellington, Charles Porter. "The aerodynamics of hovering insect flight. I. The quasi-steady analysis." *Philosophical Transactions of the Royal Society of London. B, Biological Sciences* 305, no. 1122 (1984): 1-15. https://doi.org/10.1098/rstb.1984.0049
[28] Alexander, David E. *Nature's flyers: birds, insects, and the biomechanics of flight*. JHU Press, 2002.
[29] Arora, Nipun, C-K. Kang, Wei Shyy, and A. Gupta. "Analysis of passive flexion in propelling a plunging plate using a torsion spring model." *Journal of Fluid Mechanics* 857 (2018): 562-604. https://doi.org/10.1017/jfm.2018.736
[30] Ladd, Anthony JC. "Numerical simulations of particulate suspensions via a discretized Boltzmann equation. Part 1. Theoretical foundation." *Journal of fluid mechanics* 271 (1994): 285-309. https://doi.org/10.1017/S0022112094001771
[31] He, Xiaoyi, and Li-Shi Luo. "A priori derivation of the lattice Boltzmann equation." *Physical Review E* 55, no. 6 (1997): R6333. https://doi.org/10.1103/PhysRevE.55.R6333
[32] Chen, Shiyi, and Gary D. Doolen. "Lattice Boltzmann method for fluid flows." *Annual review of fluid mechanics* 30, no. 1 (1998): 329-364. https://doi.org/10.1146/annurev.fluid.30.1.329
[33] Succi, Sauro. *The lattice Boltzmann equation: for fluid dynamics and beyond*. Oxford university press, 2001. https://doi.org/10.1093/oso/9780198503989.001.0001
[34] Lallemand, Pierre, and Li-Shi Luo. "Lattice Boltzmann method for moving boundaries." *Journal of Computational Physics* 184, no. 2 (2003): 406-421. https://doi.org/10.1016/S0021-9991(02)00022-0
[35] Arora, Nipun, Amit Gupta, and Wei Shyy. "A shifting discontinuous-grid-block lattice Boltzmann method for moving boundary simulations." *Computers & Fluids* 125 (2016): 59-70. ttps://doi.org/10.1016/j.compfluid.2015.11.003
[36] Arora, Nipun, Amit Gupta, Sanjeev Sanghi, Hikaru Aono, and Wei Shyy. "Lift-drag and flow structures associated with the “clap and fling” motion." *Physics of Fluids* 26, no. 7 (2014). https://doi.org/10.1063/1.4890221
[37] Busse, Friedrich H. "Non-linear properties of thermal convection." *Reports on Progress in Physics* 41, no. 12 (1978): 1929. https://doi.org/10.1088/0034-4885/41/12/003
[38] Aidun, Cyrus K., Yannan Lu, and E-Jiang Ding. "Direct analysis of particulate suspensions with inertia using the discrete Boltzmann equation." *Journal of Fluid Mechanics* 373 (1998): 287-311. https://doi.org/10.1017/S0022112098002493